*Kovove Mater. 53 2015 187–197*
*DOI: 10.4149/km_2015_3_187*



# Directional solidification of a TiAl alloy by combined Bridgman and power-down technique

R. P. Mooney[1], U. Hecht[2], Z. Gabalcová[3], J. Lapin[3], S. McFadden[1]*

[1] *Trinity College Dublin, Dublin 2, Ireland*
[2] *ACCESS e.V., Intzestr. 5, D-52072 Aachen, Germany*
[3] *Institute of Materials and Machine Mechanics, Slovak Academy of Sciences, Racianska 75, 831 02 Bratislava, Slovak Republic*

Received 13 April 2015, received in revised form 17 April 2015, accepted 22 April 2015

**Abstract**

TiAl alloys are of interest to the aerospace and automotive industries (particularly for engine components) on account of their relatively low density and good mechanical properties at high temperatures. Processing routes involve melting and solidification of the alloy and require knowledge about the solidification morphology and microstructural texture evolution in the component. Among others, the Columnar-to-Equiaxed Transition (CET) of bcc $\beta$(Ti) dendrites is an issue of current interest. This article examines the results from solidification experiments where a combined Bridgman and power-down technique was implemented at four different cooling rates, using cylindrical samples of the TiAl alloy: Ti-45.5Al-4.7Nb-0.2C--0.2B (all at.%). Axial CET was observed in one of the samples and axial columnar to radial columnar microstructural transitions were observed in the others. A Bridgman Furnace Front Tracking Model (BFFTM), tailored specifically for use with the experiment apparatus, was used to estimate the transient thermal conditions and columnar growth conditions for CET and other microstructural transitions. An important link, due to the nature of the power-down technique, between the reversal of radial heat flow in the hot zone of the furnace and unwanted radial columnar growth, is explained using the model. Recommendations are made on how to avoid such growth, *viz.* use of low cooling rates and large sample diameters.

K e y w o r d s: power-down technique, Bridgman furnace, gamma titanium aluminide, columnar to equiaxed transition, radial growth

*Nomenclature*

$A$ – cross sectional area ($mm^2$)
$c$ – specific heat capacity at constant pressure ($J\,kg^{-1}\,\,℃^{-1}$)
$C_0$ – original alloy composition (at.%)
$E$ – latent heat generated per unit volume ($W\,m^{-3}$)
$G$ – axial temperature gradient ($℃\,mm^{-1}$)
$h$ – heat transfer coefficient ($W\,m^{-2}\,℃^{-1}$)
$p$ – perimeter (mm)
$Q$ – heat flow (W)
$r$ – radius (mm)
$t$ – time (s)
$T$ – temperature (℃)
$u$ – pulling rate ($mm\,s^{-1}$)
$V_{tip}$ – growth rate ($mm\,s^{-1}$)
$x$ – axial position (mm)
$X$ – axial position with respect to the columnar dendrite tip (mm)
$\Delta T_{tip}$ – dendrite tip undercooling (℃)
$\rho$ – density ($kg\,m^{-3}$)

*Sub-scripts*
H – hot zone
l – liquidus
s – solidus
tip – dendrite tip
$\infty$ – infinity (far away)

*Corresponding author: tel.: +353-1-896-1359; fax: +353-1-679-5554; e-mail address: shaun.mcfadden@tcd.ie

## 1. Introduction

At the turn of the millennium Loria [1] described how gamma titanium aluminide ($\gamma$-TiAl or TiAl) alloys were emerging as new structural materials—particularly in aerospace and automotive applications—on account of their good mechanical properties at high temperature and low density. Dimiduk [2] outlined this advantage using cross plots of materials properties [3] to compare density normalised mechanical properties of TiAl with those of well-established materials. Both of these studies [1, 2] predicted that approximately 10 to 15 years of technology maturation would be required for successful implementation of TiAl in real applications.

More recently, Bewlay et al. [4] described the development of TiAl alloys in commercial aircraft engine applications and how a 2$^{nd}$ generation TiAl multicomponent alloy (Ti-48Al-2Cr-2Nb, all at.%) is in service as a low pressure turbine blade in the GEnx (General Electric's next generation) aero engine. The GEnx is used to power Boeing's 787 Dreamliner aircraft. Rising fuel costs have led to higher engine efficiency targets for engine manufacturers and hence higher engine operating temperature requirements [4]. Third generation TiAl alloys, containing a higher quantity of niobium or molybdenum, can address these demands by increasing the maximum application temperature—limited by creep resistance—from 700 ℃ (for 2$^{nd}$ generation TiAl alloys) to 850 ℃ [5]. Also, TiAl alloys can be used to reduce emmissions in commerical aircraft engines applications [6]. Other current and developing applications include engine valve trains and turbocharger rotors for the automotive industry [7].

Several processing technologies are capable of producing parts from TiAl alloys, among them; investment casting [8], electron beam melting or EBM [9], and forging with advanced machining [10], the latter using pre-shaped cast feedstock. Accordingly, the materials properties in the liquid state and the solidification behaviour of TiAl alloys with respect to morphology, microsegregation and texture formation are current research topics with wide impact on future alloy development and process engineering.

This article refers to the solidification morphology of $\beta$(Ti) dendrites in a 3$^{rd}$ generation multicomponent TiAl based alloy (hereafter referred to as 'alloy 455') and specifically to the critical growth conditions for Columnar to Equiaxed Transition (CET) that may occur during transient solidification. While the CET phenomenon and various equiaxed nucleation models have been discussed in literature [11, 12], only a few investigations focus on TiAl alloys [13, 14]. This is due to the experimental difficulties presented by handling the highly reactive melt and also because solidification patterns are easily lost, i.e., being overrun by solid state transformations. Another experimental difficulty arises where unwanted radial temperature gradients lead to radial columnar growth instead of equiaxed growth at the expected location of CET. We discuss these issues with reference to experiments performed in a Bridgman furnace by Lapin et al. [15] where traditional Bridgman solidification is combined in series with a power-down method over a range of cooling rates. A columnar front tracking model, tailored specifically for the experimental furnace set-up (in terms of heat transfer coefficients) and the applied growth conditions by Mooney et al. [16], is used to interpret the experimental results.

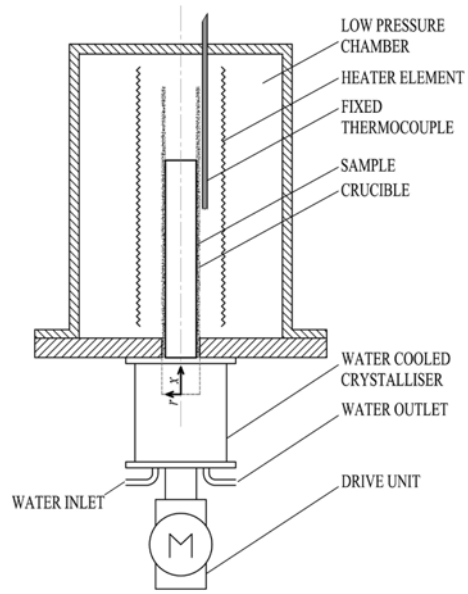


Fig. 1. Schematic of the Bridgman furnace apparatus.

The article is structured as follows: Section 2 contains details of the experimental set-up, the sample analysis procedure and the numerical model; Section 3 gives the experimental and numerical modelling results; Section 4 provides a discussion on the experimental results observed in conjunction with the simulated numerical results; and finally, Section 5 provides conclusions.

## 2. Methodology

In this section, a brief summary is given of the experiment apparatus, experiment procedure and subsequent sample analysis, as carried out by Lapin et al. [15]. This is followed by a description of the numerical model used to simulate the experiments.

### *2.1. Experimental apparatus*

Figure 1 shows a schematic of the Bridgman fur-

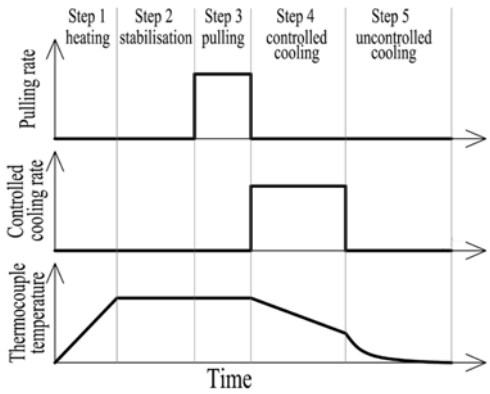


Fig. 2. Schematic plot of the process signals: pulling rate, controlled cooling rate, and thermocouple temperature, all versus time for the experimental procedure.

nace apparatus used in the experiments. The furnace is fully described by Lapin and Gabalcová [14]. The hot zone of the furnace was comprised of a cylindrical molybdenum resistance heating element (300 mm in length and 33 mm in inside diameter) contained in a sealed low-pressure chamber. The hot and cold zones of the furnace were separated by a 5-mm thick annular baffle and a 2-mm gap (on the hot side). The cold zone consisted of a water-cooled 'crystalliser' having an inside diameter of 16 mm. Samples, 150 mm in length, were contained in a 2.5-mm thick yttrium oxide crucible. A fixed thermocouple, present near the outside wall of the crucible, was used to measure and control the furnace temperature.

### 2.2. Experimental procedure

The experiments were carried out under an argon atmosphere at constant absolute pressure of 10 kPa. The following five steps describe the procedure used:

– Step 1 (heating): the sample was heated until the fixed thermocouple read 1720 ℃.

– Step 2 (stabilisation): the sample was allowed to stabilise at this temperature for 300 s.

– Step 3 (pulling): the sample—initially located as shown in Fig. 1, i.e., the cold end of the sample in line with the top of the water-cooled crystalliser—was pulled a distance of 20 mm into the crystalliser at a constant pulling rate of $2.78 \times 10^{-4}$ m s$^{-1}$.

– Step 4 (controlled cooling): the furnace temperature was decreased in a controlled manner at a fixed cooling rate from 1720 to 1420 ℃.

– Step 5 (uncontrolled cooling): the furnace was allowed to cool to room temperature without controlling the cooling rate.

This procedure was performed at four controlled cooling rates (step 4): 15, 20, 30, and 50 ℃ min$^{-1}$, as such, the controlled cooling rate was the defining process parameter that distinguishes each experimental run. Figure 2 illustrates the experimental procedure steps by showing typical process signals for pulling rate, controlled cooling rate and thermocouple temperature versus time during each step.

Note that Step 3 is the typical 'Bridgman mode' of solidification, used here to induce initial columnar grain growth, while Step 4 is the typical 'power-down mode'. The pulling rate is the speed at which the crucible is moved through the furnace. (Incidentally, due to the transient nature of the experiment, it is shown later that the growth rate of columnar grains never equates to the pulling rate of the sample.)

### 2.3. Sample analysis

The sample post-mortem analysis was carried out by optical microscopy. Chemically-etched samples were polished and examined under the stereo-microscope using; firstly, a grazing light at an approximate angle of 45° rotated into various positions to reveal each individual grain, and secondly, under flat light at 0° with the light beam parallel to the flat surface thereby revealing the primary dendrite structure (original $\beta$-phase) within each grain. The $\beta$-phase dendrite structure was used to distinguish columnar growth in the axial direction, columnar growth in the radial direction and equiaxed growth (if any) in each sample. The alloy composition was determined by chemical analysis using inductively coupled plasma (ICP) mass spectrometry and hot extraction.

### 2.4. Numerical model

The Bridgman Furnace Front Tracking Model (BFFTM)—described by Mooney et al. [17]—is a hybrid 1-dimensional transient model for axial heat flow in a cylindrical sample, solidified using the Bridgman method, where heat can be gained or lost radially at the circumference of the sample. The model uses an explicit finite difference control volume (CV) method to solve the following heat equation for temperature in a cylindrical rod of cross-sectional area $A$ and perimeter $p$, moving at a pulling rate $u$:

$$\frac{\partial}{\partial t}(\rho c T) = \\ = \frac{\partial}{\partial x}\left(k\frac{\partial T}{\partial x}\right) - u\rho c\frac{\partial T}{\partial x} - \frac{hp}{A}(T - T_\infty) + E, \quad (1)$$

where $\rho$, $c$ and $k$ are the density, specific heat capacity and thermal conductivity of the rod material, respectively; $T_\infty$ is the temperature of the surrounding source (or sink), and $E$ is the latent heat generated per unit volume. A heat transfer coefficient, $h$, applies to the radial heat flow at the circumference of the sample. (The BFFTM was recently verified by Mooney and McFadden [18].)

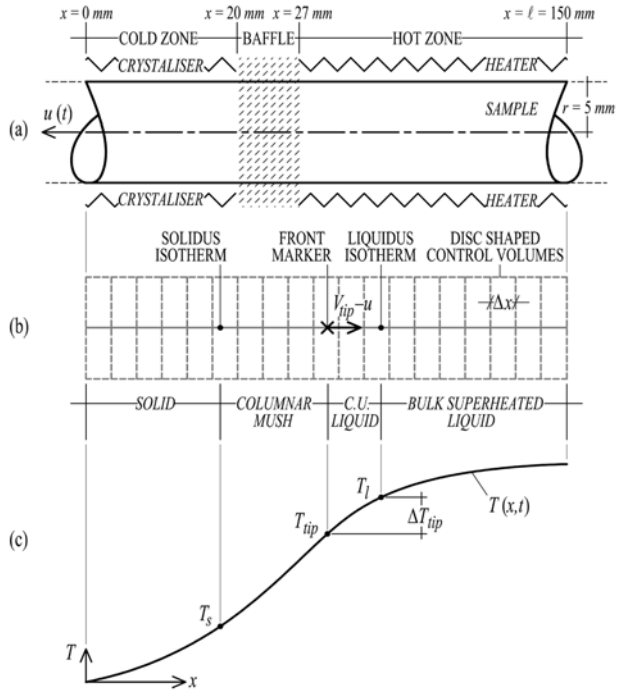


Fig. 3. (a) The physical model and (b) the numerical model of the Bridgman furnace apparatus aligned with (c) a typical sample temperature profile result.

Figure 3 illustrates how the model is applied to the experimental apparatus. Figure 3a shows a schematic drawing of the physical aspects and geometry of the furnace: the cold zone (crystalliser), the baffle and air gap region (shown hatched), the hot zone (heater), and the cylindrical sample moving at some pulling rate, $u$, as a function of time.

Figure 3b shows the numerical features of the BFFTM as applied to this physical scenario. A fixed grid of disc-shaped control volumes (CVs), each of width $\Delta x$, make up the numerical domain that encompass the length of the sample. The front marker position denotes the estimated location of the columnar dendrite tips, which have a growth rate, $V_{\mathrm{tip}}$. This growth rate is calculated as a function of columnar dendrite tip undercooling, $\Delta T_{\mathrm{tip}}$, which is given by the difference between the equilibrium liquidus temperature for the alloy, $T_{\mathrm{l}}$, and the dendrite tip temperature, $T_{\mathrm{tip}}$. The new front marker position, $x_{\mathrm{new}}$, is updated over the numerical time step, $\Delta t$, by integrating the growth vector. The growth vector is the sum of the pulling rate and columnar growth rate (which act in opposing directions); hence,

$$x_{\mathrm{new}} = x_{\mathrm{old}} + (V_{\mathrm{tip}} - u)\Delta t, \qquad (2)$$

where $x_{\mathrm{old}}$ is the previous marker position.

Figure 3c shows a typical result for the temperature profile in a sample as produced by the model at some instance in time. The dendrite tip undercooling is due, primarily, to constitutional effects in the liquid. This is the constitutional undercooling, after Tiller et al. [19]. The extent of constitutionally undercooled liquid in the figure is shown as *C.U. LIQUID* and is given by the distance between the front marker and the equilibrium liquidus temperature isotherm. Liquid ahead of this isotherm is known as *BULK SUPERHEATED LIQUID*. The extent of the dendritic *COLUMNAR MUSH* is given by the distance from the front marker back to the position of the solidus isotherm, and material at a temperature below this isotherm is fully *SOLID*. The model predicts the thermal history in the sample, $T(x,t)$, and the columnar growth conditions, tip temperature, tip undercooling, temperature gradient and growth rate.

Mooney et al. [17] performed a detailed thermal characterisation of the same Bridgman furnace apparatus described here; heat transfer coefficients were determined specifically for this furnace as a function of axial position.

The material properties, numerical parameters, geometrical properties and boundary conditions, for the simulations presented in this article, were set as per the study by Mooney et al. [16], with the exception of sample length which was 20 mm shorter at 150 mm. The latent heat evolution is governed by a solid fraction to temperature relationship, which was generated by THERMOCALC, also given by Mooney et al. [16].

## 3. Results

### 3.1. Experiment results

Following the sample microstructure analysis by stereoscope microscope, it was possible to identify distinct growth patterns of the primary $\beta$-phase. Figure 4 shows section images of the etched and polished samples, where sample I was cooled at 15 °C min$^{-1}$, sample II was cooled at 20 °C min$^{-1}$, sample III was cooled at 30 °C min$^{-1}$, and sample IV was cooled at 50 °C min$^{-1}$. In each sample the predominant growth pattern(s) of the primary $\beta$-phase was identified and the transition between each region is given by a solid white line in the figure. Regions marked 'U' were unmelted during the procedure, regions marked 'C' had axial columnar growth, regions marked 'R' had radial columnar growth, and regions marked 'E' had equiaxed growth. In three of the samples—samples I, II and IV in Fig. 4—more than one of each growth structure coexisted along the length of the sample. For example, sample I exhibited a region (from 70 mm to 115 mm, marked 'C R E') where axial columnar, radial columnar, and equiaxed grains coexisted. In samples II and IV axial columnar growth existed alongside radial columnar growth, which eventually choked the axial

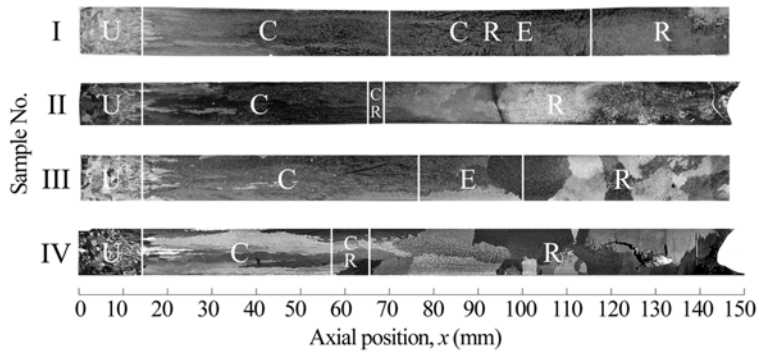


Fig. 4. Images of etched and polished samples (numbered I–IV) with primary $\beta$-phase microstructure regions identified as follows: U – unmelted, C – axial columnar, R – radial columnar, and E – equiaxed.

Table 1. Experiment results

| | Experiment/Sample No. | | | | | | | |
|---|---|---|---|---|---|---|---|---|
| | I | | II | | III | | IV | |
| Controlled cooling rate (°C min$^{-1}$) | 15 | | 20 | | 30 | | 50 | |
| Transition position (mm) | 70 | 115 | 65 | 68 | 76 | 100 | 57 | 65 |
| Transition type (& marker) | C to C R E (↑) | C R E to R (♦) | C to C R (↑) | C R to R (♦) | C to E (CET) | E to R | C to C R (↑) | C R to R (♦) |

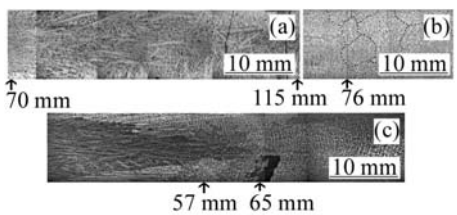


Fig. 5. Detailed images of samples I (a), III (b), and IV (c).

growth. These regions are marked 'C R'. The positions of each microstructural transition shown in Fig. 4 are listed in Table 1, with the exception of the 'U' to 'C' transition which was approximately the same for each sample at 14 mm.

Figure 5a shows a detailed image of the 'C R E' region from sample I; Fig. 5b shows the 'C' to 'E' transition from sample III; and Fig. 5c shows the 'C', 'C R', and 'R' regions in sample IV.

Finally, the chemical analysis of the alloy samples by ICP and hot extraction returned the following alloy composition: Ti-45.5Al-4.7Nb-0.2C-0.2B (all at.%).

### *3.2. Numerical results*

The BFFTM simulated the conditions at the dendrite tip, namely, undercooling ($\Delta T_{\mathrm{tip}}$), growth rate ($V_{\mathrm{tip}}$), and temperature gradient ($G_{\mathrm{tip}}$), throughout the solidification process. Table 2 gives the simulated values for these variables at the *axial columnar* microstructural transitions. Since the model only simulates axial columnar growth, the model may only be used to interpret solidification conditions occurring during axial columnar growth and at the subsequent transition from the axial columnar structure (top row of data in Table 2).

This approach of modelling and analysing axial columnar growth in the absence of equiaxed solidification modelling is called the 'indirect' approach and was successfully applied to CET analysis by McFadden et al. [20]. Discussion on direct and indirect approaches to solidification analysis are available in McFadden et al. [21]. The simulated undercooled width for each axial columnar transition is also given in Table 2, i.e., the width of constitutionally undercooled liquid ahead of the columnar front at the moment the transition occurred.

The evolution of dendrite tip growth rate, and corresponding tip undercooling, are plotted against front position in Fig. 6 and Fig. 7, respectively.

Figure 8 shows dendrite tip growth rate plotted against temperature gradient at the dendrite tip. This graph is frequently used in CET modelling when a Hunt analysis [22] is performed. Each plot on the graph is a locus of temperature gradient and growth

Table 2. Numerical results

| | Simulation No. | | | |
|---|---|---|---|---|
| | I | II | III | IV |
| Axial columnar transition position (mm) | 70 | 65 | 76 | 57 |
| $\Delta T_{\text{tip}}$ (°C) | 3.3 | 3.3 | 4.0 | 3.8 |
| $V_{\text{tip}}$ (mm s$^{-1}$) | 0.0730 | 0.0739 | 0.128 | 0.1171 |
| $G_{\text{tip}}$ (°C mm$^{-1}$) | 2.073 | 2.957 | 1.089 | 3.876 |
| Undercooled width (mm) | 1.6 | 1.1 | 3.7 | 1.0 |

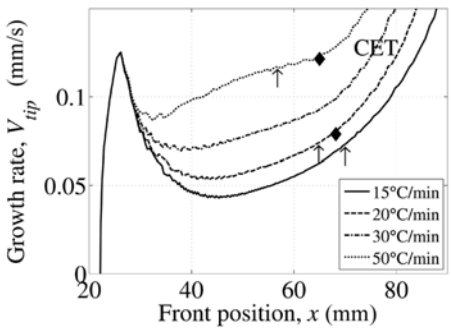


Fig. 6. Dendrite tip growth rate versus front position.

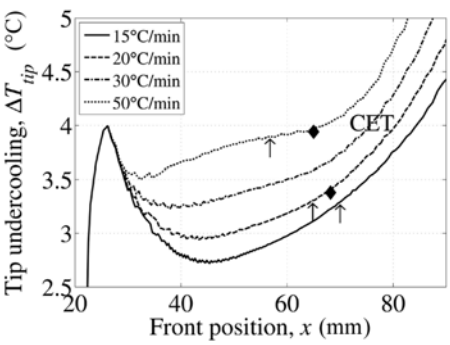


Fig. 7. Dendrite tip undercooling versus front position.

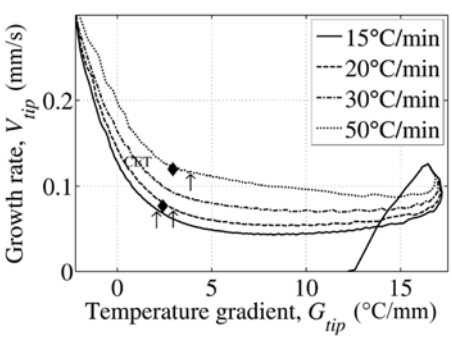


Fig. 8. Dendrite tip growth rate versus temperature gradient.

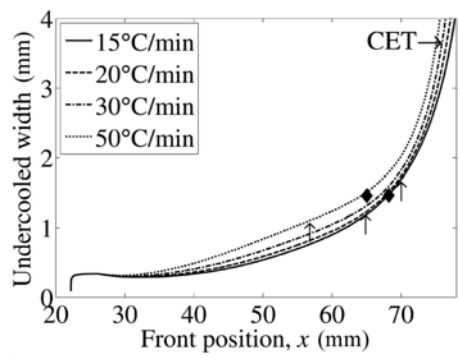


Fig. 9. Undercooled region width versus front position.

rate evolution at the columnar tips. Each plot in Fig. 8 should be interpreted by following the loci (all of which start on the $x$-axis) initially travelling from left to right before looping around in a clockwise direction, and continuing from right to left in the general direction towards the $y$-axis of the graph.

Finally, Fig. 9 shows a plot of the undercooled width (extent of bulk undercooled liquid ahead of the marker) versus front position. The transition type markers ('↑', '♦' and 'CET') listed in Table 1 are included in each figure to demarcate the principal microstructural transitions observed in each experiment. As noted previously, the numerical model simulates axial columnar growth only, i.e., the model is valid up to and including the initial marker locations (arrow or CET marker).

## 4. Discussion

### 4.1. Summary of experiment results

Only the dendritic primary $\beta$-phase was considered in the sample analysis. All of the samples revealed a distinguishable unmelted region approximately 14 mm long, labelled 'U' in Fig. 4, followed by period of columnar growth in the axial direction of the furnace, labelled 'C' in this figure. Columnar to equiaxed transition was observed in only one of the four experimental

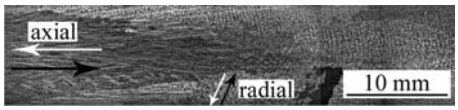


Fig. 10. Axial and radial columnar growth (black arrows) and corresponding axial and radial heat flow directions (white arrows), in the sample cooled at 50 °C min$^{-1}$.

samples (Fig. 4, image III) where the controlled cooling rate was 30 °C min$^{-1}$.

Columnar growth in the radial direction, i.e., emanating from the circumference of the crucible, was observed in the samples cooled at 20 and 50 °C min$^{-1}$. This led to 'choking' of axial columnar growth in these samples so that only radial columnar microstructure was prevalent during the latter stages of solidification. Figure 5c is reproduced above with annotations (Fig. 10) to illustrate an example of such an occurrence. Axial columnar growth is overcome by radial columnar grains that appear to have nucleated at the circumference of the sample during solidification.

In the sample cooled at 15 °C min$^{-1}$, axial columnar, radial columnar and equiaxed microstructures coexisted for a significant length of the sample until, eventually, a fully radial columnar microstructure was observed.

Similar results are found in the literature in directional solidification experiments using a TiAl alloy of similar composition to that used in the experiments here. Mooney et al. [23] describe how radial columnar growth prevented the possibility of CET in power-down experiments on board the MAXUS-8 sounding rocket. Kartavykh et al. [24] present terrestrial experiment results showing centreline segregation in cylindrical samples owing to radial temperature gradients.

### *4.2. Radial columnar growth*

In directional solidification experiments using the Bridgman or power-down method, nucleation events at the circumference of the mould wall are an unwanted phenomenon. If the conditions allow, columnar grain growth in the radial direction can occur and subsequently interfere with the progress of columnar growth in the axial direction. In columnar grain growth, the preferred growth direction ⟨100⟩ is opposite to that of the heat flow. Figure 10 illustrates this, where the growth direction is shown by black arrows and the heat flow direction is indicated by white arrows.

When a Bridgman furnace is used for directional solidification, a positive axial temperature gradient is desired so that heat flow occurs in the negative $x$-direction (referring to the coordinate system in Fig. 1). In other words, when $\mathrm{d}T/\mathrm{d}x > 0$ heat flows axially to

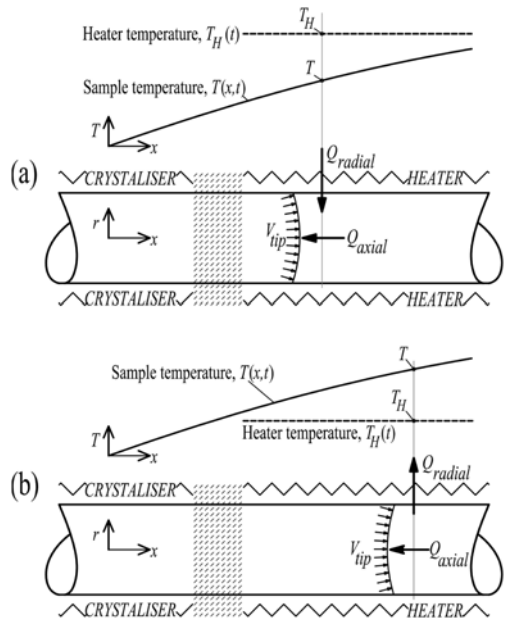


Fig. 11. Effect of radial heat flow direction on front shape: (a) desirable convex front shape, (b) unfavourable concave front shape.

the cold zone (crystalliser). If a concurrent radial temperature gradient occurs at any axial position in the sample, i.e., $\mathrm{d}T/\mathrm{d}r \neq 0$, where $r$ is the sample radius, heat may also flow in the radial direction. In this case, if $\mathrm{d}T/\mathrm{d}r > 0$ heat will flow radially into the sample from the surroundings and, conversely, if $\mathrm{d}T/\mathrm{d}r < 0$ heat will flow from the sample to the surroundings. Note that, in accordance with Fourier's law, the direction of the axial ($Q_{\mathrm{axial}}$) and radial ($Q_{\mathrm{radial}}$) heat components occur in opposition to the sign of their respective temperature gradients.

Considering, from the point of view of an axial section through the sample, the 2-dimensional shape of the columnar front that joins all the columnar dendrite tips; the sign of the radial heat flow component will influence this shape. A simple thought experiment shows that when both $\mathrm{d}T/\mathrm{d}r$ and $\mathrm{d}T/\mathrm{d}x$ are positive, one would expect a convex front shape, which will suppress radial columnar growth. This is illustrated in Fig. 11a. Conversely, when $\mathrm{d}T/\mathrm{d}x$ is positive and $\mathrm{d}T/\mathrm{d}r$ is negative, one would expect a concave front shape which promotes radial columnar growth, as in Fig. 11b. The latter case corresponds to the scenario observed in Fig. 10, and as such is the undesirable case.

The BFFTM assumes that the temperature in a CV does not vary in the radial direction. It does, however, account for heat flow at the circumference of the CV, i.e., radial heat flow. This approach is suitable for situations, like ours, with a low Biot number (less than 0.1). The direction of the axial and radial heat

Table 3. Simulated positions of radial heat flow reversal

| | Simulation No. | | | |
|---|---|---|---|---|
| | I | II | III | IV |
| Position of radial flow reversal (mm) | 63.0 | 58.8 | 52.9 | 46.0 |

flow components—as predicted by the model—can be used to predict the most likely front shape to occur during solidification.

When the cooling phase begins the front is located at an axial location of approximately 25 mm, i.e., in the baffle region. Soon thereafter, the front moves into the hot region of the furnace (at 27 mm). At this point—in all simulations—the axial heat flow component, $Q_{\text{axial}}$, occurs in the negative $x$-direction, i.e., heat flows axially towards the cold zone, and $Q_{\text{radial}}$ occurs in the negative $r$-direction, i.e., heat is received by the CV from the surroundings. This scenario is conducive to a convex (desirable) front shape, as illustrated in Fig. 11a.

In the early stages of solidification, the front shape progresses in this convex manner. As cooling progresses, and the solidification front moves through the hot zone, at some point (due to the controlled cooling) the heater becomes cooler than the sample itself, $T_{\text{H}} < T$. In this case, the radial heat flow changes sign, and now radial heat flow is from the sample to the heater, i.e., $Q_{\text{radial}}$ is in the positive $r$-direction. This is illustrated in Fig. 11b. The BFFTM was used to determine the axial location at which the radial heat flow component—in the CV containing the front—changes sign, i.e., the position of radial heat flow reversal. The results of this exercise are given in Table 3. Three observations were made clear by this analysis: (1) radial heat flow reversal occurred in all samples, (2) the timing of the radial heat flow reversal lagged behind the moment the furnace switched from Bridgman to power-down mode, (3) radial heat flow reversal occurred earlier and closer to the cold zone as the cooling rate was increased.

No direct correlation is found by comparing radial heat flow reversal predictions with the onset of radial growth in the microstructures. It is considered that at the instant radial heat flow reverses, a zero radial gradient exists, and this should favour a flat solidification front. The radial growth will require some nucleation undercooling and a sufficient radial heat flow to initiate. It is clear, however, that the radial heat flow reversal is a prerequisite for radial growth; therefore, the radial heat flow reversal is a necessary but insufficient condition for the onset of radial columnar growth.

It is interesting to note that the thermal scenario shown in Fig. 11b is difficult to achieve in traditional steady Bridgman solidification, since the heater temperature is always higher than that of the moving sample. Martorano et al. [26] did observe, however, radial columnar growth in experiments using the Bridgman method where large changes in pulling velocity were applied, in other words, during transient solidification. Both scenarios, (a) and (b) shown in Fig. 11, are possible when using the power-down method in steady *or* transient conditions. The cooling rate influences the possibility of scenario Fig. 11a leading to scenario Fig. 11b. A low cooling rate delays the moment of radial heat flow reversal, causing it to occur further along the sample from the cold zone. A high cooling rate promotes an earlier onset of radial heat flow reversal with the reversal occurring closer to the cold zone.

A recent article, by Miller and Pollock [26], describes results from directional solidification experiments carried out using the Bridgman method with Liquid Metal Cooling (LMC) where the mould geometry was designed to promote varying solidification conditions. They observed 'lateral growth' (i.e., radial columnar growth) in two different multicomponent alloys. Simulation modelling results were used to propose a criterion for lateral growth based on front shape inclination angle. Similar to the results presented in this article, it is concluded that lateral growth is indicative of conditions for the complete breakdown of directional solidification.

### *4.3. Columnar to equiaxed transition*

A clear CET occurred in the sample cooled at $30\,^{\circ}\text{C}\,\text{min}^{-1}$. It is well established in literature that equiaxed nucleation and growth will tend to occur ahead of columnar dendrites when growing at high growth rates and at low temperature gradients [12]. A high columnar growth rate implies that sufficient undercooling exists ahead of the columnar dendrites for equiaxed nucleation to occur. Although the magnitude of the solutal undercooling at the columnar dendrite tip differs from the constitutional undercooling in the liquid ahead of the tip, under constrained growth conditions, the undercooling at the tip gives a limiting value to the peak constitutional undercooling ahead of the tip.

Figure 12 illustrates how the solutal undercooling at the tip and undercooling ahead of the tip are related. The dot-hatched region represents constitutionally undercooled liquid. In a positively partitioning system, the liquid in this region is enriched by solute rejected from the growing dendrite so that the equilibrium liquidus temperature, $T_{\text{l}}(X)$, is lower than its value for the original alloy composition, $T_{\text{l}}(C_0)$. Generally, if solutal undercooling at the columnar tip is increased or lowered, then the constitutional undercool-

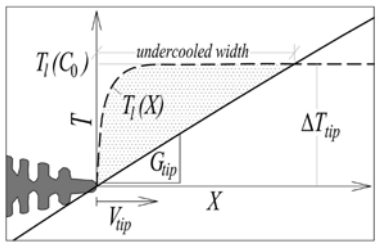


Fig. 12. The width of the undercooled region ahead of a columnar dendrite.

ing ahead of the tip is increased or lowered accordingly. In addition, if the temperature gradient decreases, then the undercooled width increases, too. Given a sufficient level of undercooling and the availability of nucleated particles in the melt, equiaxed crystals can nucleate and grow in the undercooled region ahead of the columnar tips. A low gradient will reduce the likelihood of a strong preferential growth direction, hence giving equiaxed growth.

The CET in the 30 ℃ min$^{-1}$ sample occurred at the highest columnar growth rate, $V_{\text{tip}} = 0.128$ mm s$^{-1}$, and highest columnar tip undercooling, $\Delta T_{\text{tip}} = 4.0$ ℃. However, this undercooling value is only marginally greater than the columnar tip undercooling values for the columnar to radial transitions in the other samples.

Figure 8 shows that the simulated temperature gradient is continually decreasing and approaching zero in all cases. The CET occurred at the lowest temperature gradient, $G_{\text{tip}} = 1.089$ ℃ min$^{-1}$, when compared to the other columnar transitions (ranging from 2.073 to 3.876 ℃ min$^{-1}$). The lower temperature gradient increases the width of undercooled liquid ahead of the front, which in turn increases the likelihood of equiaxed grain nucleation in the undercooled liquid. The width of undercooled liquid ahead of the front at the position of CET was larger, at 3.7 mm, than that of the other columnar transitions: 1.0 mm to 1.6 mm. This is illustrated in Fig. 9.

### *4.4. Convection in the melt*

Natural convection is defined as flow resulting from the effects of gravity on density differences, i.e., where a density gradient exists, in the liquid [27]. Such density differences in the liquid can be due to a temperature gradient (thermal convection), a concentration gradient (solutal convection), or both (thermo-solutal convection). The BFFTM does not consider heat transfer occurring due to natural convection in the liquid.

Relevant discussion is given on this topic in reference [16]. The discussion assumes that no radial temperature gradient exists in the liquid; and focusses on the fact that the crucible and sample do not move during the experimental procedure (resulting in a static columnar front). It is assumed that, since no growth is occurring, no solute is rejected at the columnar front, and any concentration gradient in the liquid has had time to equilibrate by chemical diffusion. Therefore, it is implied that no solutal convection exists. An axial thermal gradient does exist; but the gradient is aligned with the gravity vector (in a vertical Bridgman furnace), so that hotter (lower density) liquid overlays cooler (higher density) liquid, thereby providing an inherently stabilising effect on the liquid.

The situation, however, is different in the experimental procedure described in this article since the Bridgman apparatus is used for the purposes of directional solidification. While the thermal gradient is still aligned with the gravity vector, a concentration gradient in the liquid must exist during directional solidification. Whether the concentration gradient has a stabilising or destabilising effect on liquid depends on the density of solutes being rejected. The main elements contained in the solutes of alloy 455 (i.e., aluminium and niobium) both have a destabilising effect on the liquid during growth. Buoyant aluminium (less dense than titanium) is rejected at the columnar front, whilst—contrarily, but having the same effect on the density field—heavy niobium (more dense than titanium) is consumed from the melt during growth. However, partitioning is weak in both cases: $k_{\text{part}} \approx 0.9$ for Al in Ti, and $k_{\text{part}} \approx 1.1$ for Nb in Ti. For this reason, it is appropriate to say that the results obtained here may contain a margin of error due to natural convection in the melt. It should be noted that there are other mechanisms (apart from natural convection ahead of the columnar front) that can lead to convective flow in the Bridgman process. For example, flow in the mushy zone, shrinkage driven flow, and surface tension forces are leading to Marangoni convection [27]. Incorporation of convection flow mechanisms in the current model is beyond the scope of this study.

## 5. Conclusion

Following a complete microstructural evaluation of all the experiment samples, and in consideration of the primary $\beta$-phase, it was found that CET occurred in the sample cooled at 30 ℃ min$^{-1}$ only. The solidification modelling carried out explained the conditions that produced this CET, since, compared to the other microstructural transitions modelled, the CET position had the highest dendrite tip growth rate, $V_{\text{tip}} = 0.128$ mm s$^{-1}$, highest dendrite tip undercooling, $\Delta T_{\text{tip}} = 4.0$ ℃, the lowest temperature gradient, $G_{\text{tip}} = 1.089$ ℃ min$^{-1}$, and the widest undercooled region at 3.7 mm. This information is insightful since it provides an estimation of the growth conditions (to

be avoided) for CET in castings of the gamma TiAl alloy: Ti-45.5Al-4.7Nb-0.2C-0.2B (at.%). In all of the other samples the axial columnar growth was interrupted by radial columnar growth, thus, preventing the possibility of CET in those samples.

The model highlights an important consideration for CET experiment designers who intend to use the power-down method. High cooling rates lead to a situation where the heater temperature is less than that of the liquid in the sample. This subsequently leads to an unfavourable heat flow pattern that promotes radial columnar growth, thereby 'choking' undercooled liquid ahead of (axial) columnar grains and preventing the possibility of CET. Even though the radial temperature gradients in the case presented here were relatively small, the axial temperature gradient had to be reduced to a low value for CET and, ultimately, the axial and radial gradients reached a similar order of magnitude.

In conclusion, CET studies using the power-down method should utilise appropriate thermal modelling to ensure that the conditions promoting detrimental radial heat flow away from the sample in the hot zone are avoided. The use of large sample diameters and low cooling rates delays the reversal of radial heat flow that is a precursor to radial growth. However, one should be mindful that sufficient undercooling in the liquid is required to allow for the nucleation and growth of equiaxed dendrites.

## Acknowledgements

This work was carried out as part of the GRADECET (GRAvity DEpendence of Columnar to Equiaxed Transition in TiAl Alloys) research project. The authors R. P. Mooney and S. McFadden would like to thank the European Space Agency PRODEX programme for funding the research (agreement number: 4000107132) under the management of the Irish Space Delegation at Enterprise Ireland. The authors J. Lapin and Z. Gabalcová would like to acknowledge the financial support of the Slovak Research and Development Agency under the contract APVV-0434-10, the Slovak Grant Agency for Science under the contract VEGA 2/0149/13 and the Slovak Academy of Sciences under the contract of MVTS funding of ESA project GRADECET. Finally, author U. Hecht would like to acknowledge the German Federal Ministry of Research (contract: FKZ 50WM1143).

## References

[1] Loria, E. A.: Intermetallics, *8*, 2000, p. 1339. doi:10.1016/S0966-9795(00)00073-X
[2] Dimiduk, D. M.: Mater. Sci. Eng. A, *263*, 1999, p. 281. doi:10.1016/S0921-5093(98)01158-7
[3] Ashby, M. F.: Materials Selection in Mechanical Design. Oxford, Pergamon Press 1992.
[4] Bewlay, B. P., Weimer, M., Kelly, T., Suzuki, A., Subramanian, P. R.: MRS Proc., *1516*, 2013, p. 49. doi:10.1557/opl.2013.44
[5] Clemens, H., Smarsly, W.: Adv. Mater. Res., *278*, 2011, p. 551. doi:10.4028/www.scientific.net/AMR.278.551
[6] Lavery, N. P., Jarvis, D. J., Voss, D.: Intermetallics, *19*, 2011, p. 787. doi:10.1016/j.intermet.2010.11.019
[7] Appel, F., Paul, J. D. H., Oehring, M.: Gamma Titanium Aluminide Alloys: Science and Technology. Weinheim, Germany, Wiley-VCH Verlag GmbH & Co. KGaA 2011.
[8] Aguilar, J., Schievenbusch, A., Kättlitz, O.: Intermetallics, *19*, 2011, p. 757. doi:10.1016/j.intermet.2010.11.014
[9] Biamino, S., Penna, A., Ackelid, U., Sabbadini, S., Tassa, O., Fino, P., Pavese, M., Gennaro, P., Badini, C.: Intermetallics, *19*, 2011, p. 776. doi:10.1016/j.intermet.2010.11.017
[10] Tetsui, T., Shindo, K., Kaji, S., Kobayashi, S., Takeyama, M.: Intermetallics, *13*, 2005, p. 971. doi:10.1016/j.intermet.2004.12.012
[11] Hutt, J., StJohn, D.: Int. J. Cast Met. Res., *11*, 1998, p. 13.
[12] Spittle, J. A.: Int. Mater. Rev., *51*, 2006, p. 247. doi:10.1179/174328006X102493
[13] Mooney, R. P., McFadden, S., Rebow, M., Browne, D. J.: IOP Conf. Ser. Mater. Sci. Eng., *27*, 2012, p. 12020. doi:10.1088/1757-899X/27/1/012020
[14] Lapin, J., Gabalcová, Z.: Intermetallics, *19*, 2011, p. 797. doi:10.1016/j.intermet.2010.11.021
[15] Lapin, J., Gabalcová, Z., Hecht, U., Mooney, R. P., McFadden, S.: Mater. Sci. Forum, *790–791*, 2014, p. 193. doi:10.4028/www.scientific.net/MSF.790-791.193
[16] Mooney, R. P., McFadden, S., Gabalcová, Z., Lapin, J.: Appl. Therm. Eng., *67*, 2014, p. 61. doi:10.1016/j.applthermaleng.2014.02.048
[17] Mooney, R. P., McFadden, S., Rebow, M., Browne, D. J.: Trans. Indian Inst. Met., *65*, 2012, p. 527. doi:10.1007/s12666-012-0201-2
[18] Mooney, R. P., McFadden, S.: Simul. Model. Pract. Theory, *48*, 2014, p. 24. doi:10.1016/j.simpat.2014.07.005
[19] Tiller, W. A., Jackson, K. A., Rutter, J. W., Chalmers, B.: Acta Metall., *1*, 1953, p. 428. doi:10.1016/0001-6160(53)90126-6
[20] McFadden, S., Browne, D. J., Gandin, C.-A.: Metall. Mater. Trans. A, *40*, 2009, p. 662. doi:10.1007/s11661-008-9708-x
[21] McFadden, S., Browne, D. J., Banaszek, J.in Materials Science Forum, *508*, 2006, p. 325. doi:10.4028/www.scientific.net/MSF.508.325
[22] Hunt, J. D.: Mater. Sci. Eng., *65*, 1984, p. 75. doi:10.1016/0025-5416(84)90201-5
[23] Mooney, R., Browne, D., Budenkova, O., Fautrelle, Y., Froyen, L., Kartavykh, A., McFadden, S., Rex, S., Schmitz, B., Voss, D.: In: European Space Agency, (Special Publication) ESA SP, 2011, 700 SP, p. 453. ISBN: 978-92-9092-264-3.
[24] Kartavykh, A. V., Ginkin, V. P., Ganina, S. M.: J. Alloys Compd., *586*, 2014, p. 267. doi:10.1016/j.jallcom.2012.12.063

[25] Martorano, M. A., Neto, J. B. F., Oliveira, T. S., Tsubaki, T. O.: Mater. Sci. Eng. B, *176*, 2011, p. 217. doi:10.1016/j.mseb.2010.11.010

[26] Miller, J. D., Pollock, T. M.: Acta Mater., *78*, 2014, p. 23. doi:10.1016/j.actamat.2014.05.040

[27] Stefanescu, D. M.: Science and Engineering of Casting Solidification. 2nd Edition. New York, Springer 2008.